appliedoptics

Low-cost hyper-spectral imaging system using a linear variable bandpass filter for agritech applications

Shigeng Song,[1] Des Gibson,[1,*] Sam Ahmadzadeh,[1] Hin On Chu,[1] Barry Warden,[2] Russell Overend,[2] Fraser Macfarlane,[3] Paul Murray,[3] Stephen Marshall,[3] Matt Aitkenhead,[4] Damian Bienkowski,[5] and Russell Allison[6]

[1]*Institute of Thin Films, Sensors & Imaging, SUPA, University of the West of Scotland, Scotland PA1 2BE, UK*
[2]*Wideblue Ltd, Glasgow, UK*
[3]*Department Electronic and Electrical Engineering, University of Strathclyde, Royal College Building, 204 George Street, Glasgow, UK*
[4]*The James Hutton Institute, Aberdeen AB15 8QH, Scotland, UK*
[5]*The James Hutton Institute, Dundee DD2 5DA, Scotland, UK*
[6]*Galloway & MacLeod Ltd. South Lanarkshire, UK*
*Corresponding author: des.gibson@uws.ac.uk

Hyperspectral imaging for agricultural applications provides a solution for non-destructive, large-area crop monitoring. However, current products are bulky and expensive due to complicated optics and electronics. A linear variable filter was developed for implementation into a prototype hyperspectral imaging camera that demonstrates good spectral performance between 450 and 900 nm. Equipped with a feature extraction and classification algorithm, the proposed system can be used to determine potato plant health with ∼88% accuracy. This algorithm was also capable of species identification and is demonstrated as being capable of differentiating between rocket, lettuce, and spinach. Results are promising for an entry-level, low-cost hyperspectral imaging solution for agriculture applications.   © 2020 Optical Society of America

1. INTRODUCTION

Crop monitoring has been of significant importance in recent years, particularly for improved crop yield and food security. The ability to know which areas in a field require attention can prevent localized drought and spreading of disease. This is difficult to do manually considering the scale of the task, new technologies such as LiDAR and multispectral imaging are being explored to provide automated solutions for crop health monitoring at the field scale.

Multispectral and hyperspectral imaging (HSI) solutions have addressed these challenges. HSI has great potential in agriculture applications, particularly for disease detection [1–5], plant development [6], and large-area soil nutrient content monitoring [7]. These technologies also reduce the training and experience required to perform the same task manually. For example, basal stem rot (BSR) is a fatal fungal disease of palm oil plantations, and Liaghat *et al.* [1] used reflectance spectroscopy analysis in the visible to near-infrared region (325–1075 nm) to assess this disease.

This analysis determined whether the health of palm leaf samples were from healthy, slightly damaged, moderately damaged, or heavily damaged trees. Their results achieved rapid screening of BSR in palm using spectral analysis. Sankaran *et al.* [4,5] demonstrated use of visible–near-infrared and mid-infrared spectroscopy to distinguish whether citrus leaves were infected with canker, with a classification accuracy of ∼90%. Liu *et al.* (2014) [6,7] non-destructively monitored changes of chlorophyll content for field plants, using a real-time monitoring system based on visible and near-infrared reflection spectroscopy. Their investigation validated the adequate performance of spectral analysis by comparing the results with chlorophyll index determined by the standard instrumentation and indicated that reflectance at 700 nm is a sensitive indicator of chlorophyll concentration.

Linear variable filters (LVFs) provide an alternative optical system to diffraction gratings, as seen in a study by Emadi *et al.* [8], who developed a Fabry–Perot type LVF for an ultraviolet micro-spectrometer for potential applications in atmospheric gas sensing and pharmaceutical analysis. They cited an advantage from utilizing LVFs, which is that they enable fast data

capture as an LVF scans across a sensor, compared to conventional hyperspectral imaging cameras, where line-scanned images must be taken and thus the whole camera unit must move in order to acquire an image. This is particularly important for effective space and imaging time utilization. However, due to its optical assembly the spectrometer was bulky and had low sensitivity in the UV region. This makes it difficult to expand their usage, with pricing of these systems typically on the order of tens of thousands of dollars.

An issue with producing LVFs is that they are complex optical filter designs, making volume production difficult. Current LVF deposition utilizes a dynamic masking mechanism to achieve the spatial gradient [9].

This paper describes a novel LVF fabrication process that utilizes a static masking mechanism [10]. Use of static masks provides a high-throughput LVF deposition process as described in Section 2. The new process separates the film deposition and oxidation steps, as oxidation is done separately, reducing the chance of pinhole development and improving deposition rates.

This paper addresses these HSI camera issues by designing a low-cost, portable HSI camera for agritech by utilizing novel mass producible linear variable bandpass filters (LVFs) [10]. Conventional LVF manufacturing processes are typically based on dynamic masking and more complicated setups to achieve spatial gradient [11–13], which limits throughput per deposition run. A hyperspectral crop camera (HCC) was developed and prototyped that utilized these mass-producible LVFs to significantly reduce spectrometer size and cost.

2. LVF FABRICATION

A. Equipment and Process

Deposition of the LVF was carried out using a microwave-plasma-assisted pulsed-DC reactive sputtering process [10]. Mechanical masking to achieve spatial variation in the bandpass center wavelength across the substrate surface was applied. Figure 1 shows the deposition system configuration.

This employs a horizontally mounted rotating drum, where substrates are mounted with configurable flanges for target masks. A microwave-plasma source is set up at the top of the system. Film thickness was monitored with six quartz crystal microbalances.

The drum rotation speed is such that two monolayers are deposited per pass across the magnetron targets, thereby allowing full oxidation of the metal-rich sputtered film in the separate microwave-plasma region. One key advantage of the microwave plasma in this pulsed-DC reactive sputtering system is its separated sputtering and oxidation zones. Only argon gas is introduced at the target region and oxygen in the microwave-plasma zone. This provides metal-like sputtering and separated microwave-plasma-assisted oxidation, enabling high deposition rates and high-quality films with less pinholes to be achieved.

Critical deposition rate for this process has been investigated previously [14,15] with the use of an adjustable mask placed between the targets and the rotating drum in order to produce the desired LVFs. A significant advantage of a drum-produced LVF is the avoidance of curvature for the same wavelength line. Figure 2 shows an example of an LVF produced with this deposition system with $x-y$ axes. This drum-based system
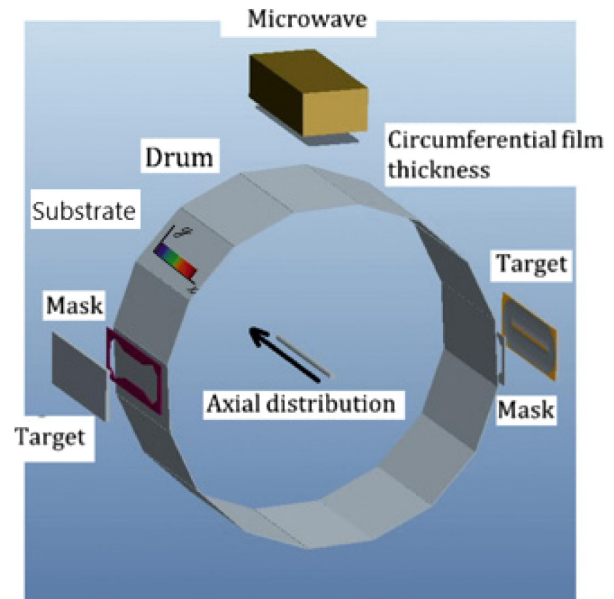

Fig. 1. Schematic of microwave-assisted pulsed-DC rotating drum sputter deposition system with a loaded substrate, mechanical masking, used to deposit novel LVFs. This shows targets, masks, the microwave, circumferential direction, and axial distribution direction.
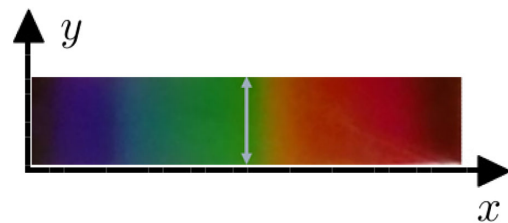

Fig. 2. Example LVF orientation, with the y axis representing the linear uniformity and the x axis representing the linear thickness gradient.

has great uniformity along the circumference of the drum and thus produces a linear thickness gradient along the x axis and uniform thickness in the transverse direction (y axis) [10].

To improve the LVF coatings, several measures were implemented, described as follows:

– Pulsed-DC sputtering is employed to suppress arcing.

– Non-microwave-assisted plasma produces molecular oxygen, whereas with the addition of microwave assistance atomic oxygen can be achieved. As a result, oxygen is more readily available to react with each layer passing by for a more uniform oxidation of the coating and therefore resulting in much improved film homogeneity.

– Deposition of a metal layer first reduces the chance of pinhole formation, allowing for a higher band of optical density films. Other deposition methods that deposit oxide materials directly are subject to pinhole formation [11–13].

– Utilizing a partial pressure controller permits for total control of oxygen partial pressure. In turn, uniform oxidization of the film can be achieved as oxygen reactivity varies through the process.

Dielectric materials used to produce the optical filter are niobium and silicon (purchased from Testbourne Ltd.; 99.99% pure and were used as received) for high/low refractive index Nb_2O_5 and SiO_2, respectively [14]. In order to produce a film with varying thicknesses across the surface, a custom uniformity mask had to be utilized. To produce such a mask for an LVF optical filter, mask design is taken into consideration [10,14,15].

B. Mask Design for Linear Gradient Thickness

A program was written to design deposition masks and calculate the desired thickness distributions for a configuration of substrates on a rotating drum, considering deposition geometry such as a target and a mask with pre-defined shape function [15].

As depicted in Fig. 3, in order to optimize the mask to achieve desired thickness distribution, several variables are considered, including: the sputtering yield, the angular distribution of the ejected particles of the target, the mask restriction function, the arriving angle of sputtered particles on the substrate, and the substrate movement.

The magnetic field was calculated and fed into the semi-empirical model to create the etch profile of the dielectric materials (targets) [15]. The etch profile is calculated by considering the integration of ion energy along the approximate ion path. By relating the magnetic field B_{tan} to the erosion track profile, a 2D data array is obtained as Trackfield. The angular distribution of ejected atoms is a function of the angle of incidence of the incident bombardment beam.

Using pulsed-DC magnetron sputtering, this angle is almost at the normal to the target surface. Considering turbulent electric field collisions, a Monte Carlo simulation determined a mean incident angle close to normal incidence for this simulation.

Angular distribution can be reduced to two unknowns, described as

$$f(\beta) = \cos(\beta - \beta_0)^n, \qquad (1)$$

where $f(\beta)$ is the angular distribution function of ejected atoms, β_0 is the angle of maximum emission, and n is a power modified distribution and is related to the target material; it can be determined through measurement and fitting [16].

For each point source, the particle arrival rate is proportional to the inverse square of r, the distance between target and substrate. $\cos(\gamma)$ corrects for the drum and substrate rotation
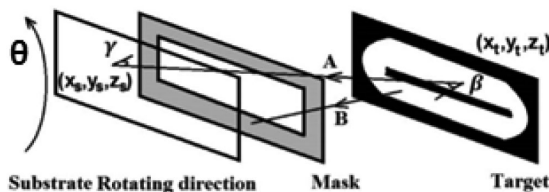

Fig. 3. Schematic of the sputtering geometry, where the substrate is mounted on a rotating drum, β is the ejected particle flux emission angle to the target surface normal, and γ is the deposited particle flux incident angle to the substrate surface normal. On path A the particle reaches the substrate, and on path B the particle is blocked by the mask. This is generated directly from the measurement of the target erosion track profile.

(γ being the angle between the beam/substrate and normal incidence). A further function passrate determines whether or not the mask blocks material arriving to the substrate:

$$probability = \frac{\cos(\beta - \beta_0)^n \times Trackfield \times passrate \times \cos(\gamma)}{r^2}. \qquad (2)$$

The target and substrate coordinates (X_t, Y_t, Z_t) and (X_s, Y_s, Z_s), respectively, are meshed with sum probabilities of all target elements determining relative thickness. Film thickness is circumferentially uniform, and therefore only two substrate coordinates are required to be derived. A specific data set is determined using coordinates X_s, $Y_{s0} - R\sin(\theta)$, $Z_{s0} - R\cos(\theta)$ for point X_s at the centerline and moved to the θ angle as shown in Fig. 3. θ is the drum rotation angle from the center of the drum and R is the drum radius. Here (X_s, Y_{s0}, Z_{s0}) are the coordinates on the rotating axis. The final relative thickness at point X_s can be obtained by integrating θ for a range of $(-\theta_0, \theta_0)$. The final equation for thickness simulation is

$$Thickness\,(X_s) = \sum_{\theta} \sum_{X_t, Y_t, Z_t} \frac{\cos(\beta - \beta_0)^n \times Trackfield \times \cos(\gamma)}{r^2}. \qquad (3)$$

Thus, using these functions with a desired thickness distribution for the LVFs, a mask geometry was designed. This was then used in the high-throughput microwave-plasma-assisted pulsed-DC reactive sputter deposition configuration to yield high-quality LVFs.

C. Deposited LVF

LVFs based on a calibration curve as described in Fig. 4 were produced as a result of optimized target mask design. This calculated shape matches the thickness distribution required to achieve the gradient structure of the deposited LVF as shown in Fig. 5.

Masked depositions have resulted in LVFs with observable distinctions between colors, as this is affected by the thickness distribution. Figure 5 shows a photograph of two LVFs produced by the aforementioned optimized process. These LVFs allow linear spectral transmission/reflection tuning along their
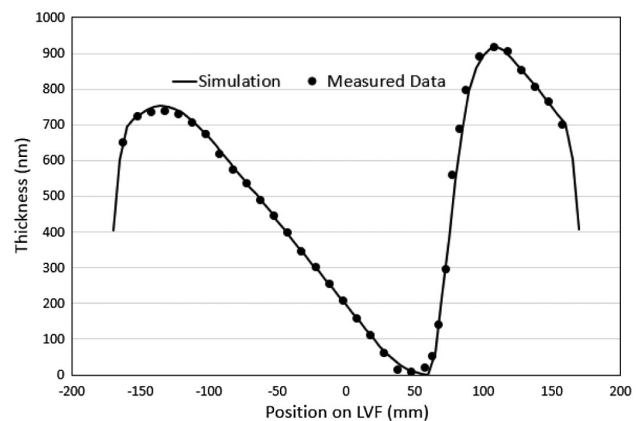

Fig. 4. Plot of the target thickness versus measured thickness as a function of LVF position. For single layer Nb_2O_5, this was a calibration curve used for determining the thickness distribution to identify positions for LVF production.
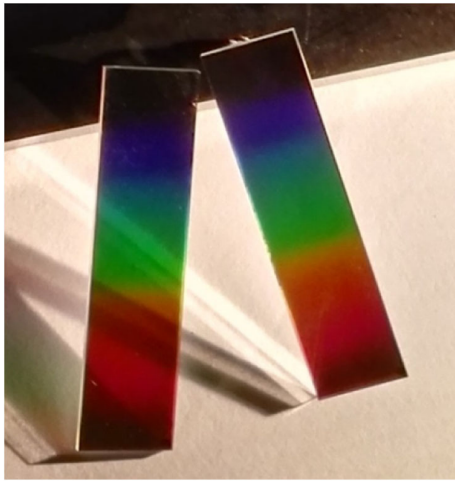
Fig. 5. Example of fabricated LVF, measuring 40×10 mm, with distinctive color gradient representing linear thickness gradient.
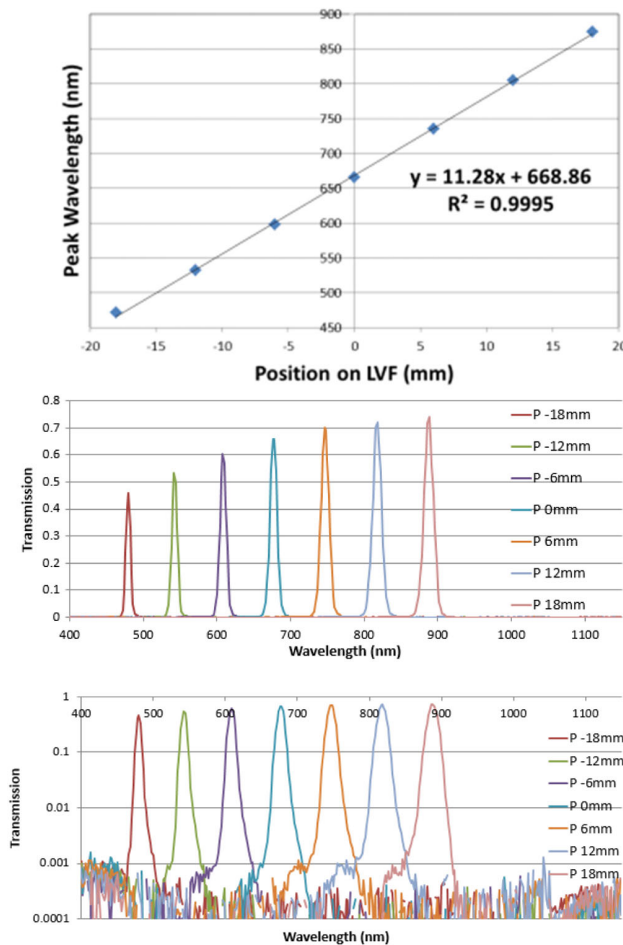

Fig. 6. Linearity, passbands, and passbands with blocking of 450–900 nm LVF.

x axis, while the optical properties remain uniform along the filters' *y* axes.

Linear variable visible bandpass filters were produced with an alternating high/low refractive index material stack.

Fifty-four layers of H/L alternating were deposited on one side, and 110 H/L alternating layers were coated on the opposite side of the substrate. Filtering was achieved by combining a wideband filter, narrowband filter, and a blocking filter over the 350–1100 nm range, which is ideal for CMOS image sensors. Optical density 3 was achieved by this combined three-filter design. FWHM was calculated to be 11.25 nm. Ultimately, high optical performance from 450 to 900 nm was achieved. Figure 6 shows the optical transmission and peak transmission wavelengths as a function of position on the LVFs. These wavelengths enable studies with multispectral and hyperspectral imaging techniques, in particular with applications in agriculture. LVF characterization was conducted using a spectrophotometer (Aquila nkd-8000) equipped with an optical fiber to produce a narrow spot size (1 mm); the filter was characterized on a motion stage.

3. NEW HYPERSPECTRAL CROP CAMERA

A. Hardware Structure and Constituents

The HCC design requires LVF position manipulation. A stepper motor with custom designed rack and pinion allowed the translation of an LVF across a standard high-spatial-resolution monochromatic image sensor (1.3MP IDS E2V CMOS Image Sensor). This creates discrete vertical strips at linearly spaced wavelengths in each image.

Figure 7 shows a basic schematic of the imaging aspects of the HCC. The LVF is located in front of the high-spatial-resolution monochromatic image sensor.

The ratio of the stepper motor gearing was selected to maximize the resolution of linear movement, where one step from the motor equated to 0.1 mm linear movement. Using this design, the LVF can be precisely translated at relatively high speed across the CMOS sensor. The HCC's internal stepper motor translation stages were designed to allow the full length of the LVF to pass the camera to allow full high-resolution spectral scanning.

The system also offers adjustable exposure times for different lighting conditions and is capable of multi-spectral and lower-spectral resolution imaging that can be achieved in less time. LVF position was controlled with an infrared optical sensor and the LVF returned to a known *home position* before each image scan. Positioning of the LVF was found to be accurate, consistent, and repeatable.

B. Wavelength Calibration

Once fully assembled, the prototype HCC was calibrated using hydrogen and helium gas discharge lamps. Discrete wavelengths of these gas discharge lamps were used to correlate step position to wavelength for the LVF. H and He were chosen, as both have several distinct emission lines in the visible spectrum. The lamps
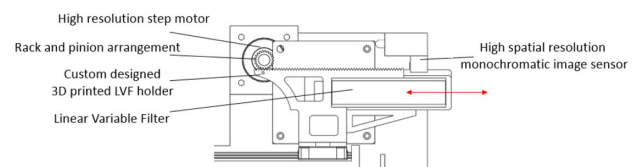

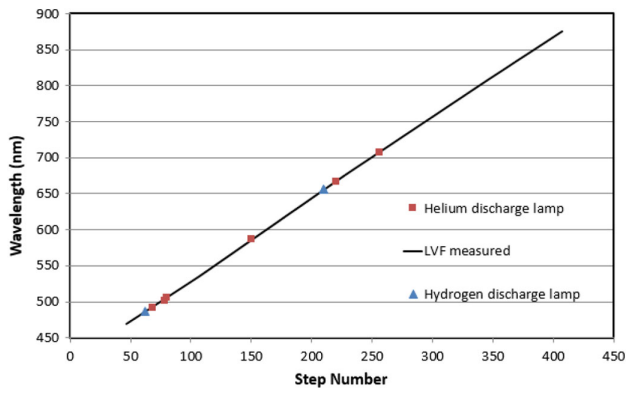**Fig. 7.** Basic components and LVF in camera set up.

Fig. 8. Shows the successful calibration of LVF step positions and correlating wavelengths (linear relation).

Fig. 9. Prototype HCC assembly with internals exposed and as a final compact design. Total volume of 150 mm × 120 mm × 100 mm, and at a weight of 650 g.

Table 1. LVF Step Position Corresponding the H and He Gas Lamp Discharge Peaks With Corresponding Step Positions

Actual Wavelength λa (nm)	Emission Line Detected at Step	Step Position Converted to Wavelength λb (nm)
486	64	488
492	70	495
501	78	506
505	80	508
587	152	586
656	210	653
667	224	665
707	260	705

were imaged using a high-resolution scan over the entire LVF spectral range from 450 to 900 nm. The expected step position was compared to the actual step position of each of the discharge lines that appeared in the calibration images.

An adjustment was then made to the starting position of the scan to bring the theoretical step position of the wavelength in line with the actual step position. Once calibrated, the device was compared to the wavelength data from the LVF. The measured LVF data was then used to create a linear plot of wavelength versus step position; see Fig. 8 and Table 1.

This plot was used to calibrate the LVF step position corresponding to the H and He gas lamp discharge peaks with corresponding step positions. Once calibrated, the H and He emission lines correspond well with the expected step position, with the error between expected wavelength and the actual wavelength measured by the HCC found to be no greater than ±5 nm.

Testing the proof-of-principle system showed good results, confirming that the manipulation of the LVF position was both accurate and repeatable.

C. Performance of the HCC

The HCC was developed as a low-cost hyperspectral imaging camera with handheld capabilities, and as part of the development of the device, the HCC was benchmarked against a high-end pushbroom hyperspectral system. For reference, the
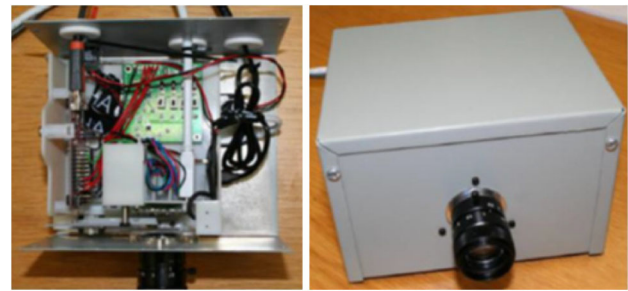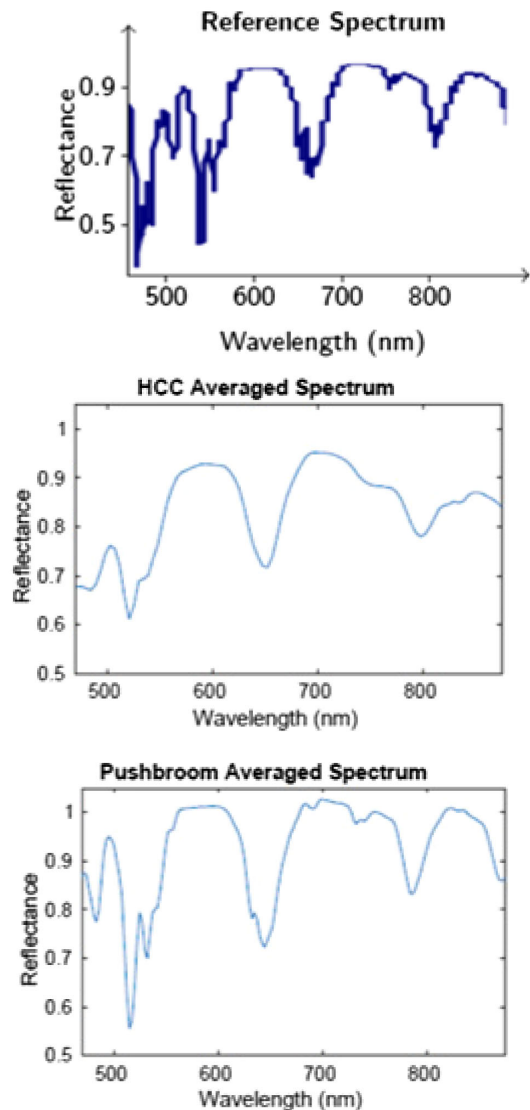

Fig. 10. Labsphere certified reflectance standard (top) was used to characterize the HCC (middle) and pushbroom (bottom) system and compared against the reference spectrum.

HCC device was approximately 1/10th the cost of the pushbroom benchmark device. Figure 9 shows the final prototype design.

Table 2.   Spectral and Spatial Resolution for Prototype and Traditional Pushbroom HSI System with Similar Settings

	Spectral Resolution	Spatial Resolution
HCC	4.53 nm	1280 × 1024
Pushbroom	2.44 nm	377 × 336

Spectra acquired by the HCC and the traditional pushbroom HSI system are highly correlated as seen in Fig. 10. Both closely resemble the manufacturer's reference spectrum in between 450 and 900 nm for a Labsphere certified reflectance standard. The spatial and spectral resolution of both systems with comparable parameter settings were compared with the results shown in Table 2.

While the spatial resolution of the HCC is far superior to that of the pushbroom system, the spectral resolution of the pushbroom system is approximately twice that of HCC when comparable settings are used. In spite of the reduced spectral resolution, as would be expected due to the device being in the prototype stage, the spectral data acquired by the HCC is accurate when compared to the reference reflectance standard and has been demonstrated to allow for accurate data acquisition.

4. DATA ANALYSIS AND CLASSIFICATION OF PLANT LIFE

A. Data Capture and Reordering

The prototype HCC camera captures images in three-dimensional hyperspectral data cubes by translating the LVF across the field of view, capturing a set of images with discrete vertical strips at linearly spaced wavelengths over subsequent steps in time. As a result, the spatial and spectral information is spread over multiple successive images. This method of capturing hyperspectral data is known as spatio-spectral imaging.

A reordering algorithm was developed in order to manage camera data segments into wavelength-dependent images for analysis. This was done in order to obtain a more traditional representation of a hyperspectral data cube, where each wavelength is contained in one plane and each successive frame represents the increasing wavelength. With this reordering algorithm, the data captured using the HCC is equivalent to that captured using a traditional pushbroom sensor.

In order to validate the HCC's usefulness in crop monitoring and classification, two distinct data sets were acquired using the system. The first consisted of images containing three types of salad leaves and was intended to determine whether or not images captured using the HCC would be sufficient for differentiating these species. The second data set consisted of selected leaves collected from potato trial fields at the James Hutton Institute (Invergowrie, UK), where selected plants had been exposed to late blight, a common disease in potato crops.

These data sets were then processed using support vector machine (SVM) classification, where, for Data set 1, a multiclass SVM was used to determine the species of leaves, and, for Data set 2, a binary SVM was used to differentiate between healthy and unhealthy areas on the leaves.

B. Feature Extraction and Dimensionality Reduction

Regions of interest (ROIs) were extracted from the image by visual inspection. After ROIs had been determined, the relevant spectra were extracted and class labels assigned. *Standard normal variate* (SNV) is a common tool in hyperspectral data pre-processing Refs. [17,18]. SNV was applied to correct for noise and scatter effects and can be defined as

$$x_i(\text{SNV}) = \frac{x_i - \overline{x_i}}{\sigma_{xi}}, \tag{4}$$

where a spectrum $x_{i,j}$, in the raw data, is normalized by subtracting its mean value $\overline{x_{i,j}}$ before being divided by the standard deviation $\sigma_{xi,j}$ of the spectra.

This process creates a set of spectra where the average of each spectrum is zero with variance of 1.

Employing SNV normalization supresses non-uniformity and inconsistencies in the data caused by undesired changes in illumination or noise scattering. With a normalized intensity, like pixels with similar spectra should be classified similarly despite the differences in original illumination. As can be seen in Fig. 11, SNV leads to a narrowing and reduction of noise primarily in the 700–800 nm region between the intensity versus wavelength (top) and normalized intensity versus wavelength (bottom) curves.

Principal component analysis (PCA), also known as the discrete Karhunen–Loève Transform or the Hotelling Transform [19], can be used for both feature extraction and dimensionality reduction, making it a common statistical technique used in HSI analysis [20]. PCA computes the covariance matrix from the SNV normalized data cube. Eigenvalues and eigenvectors can be extracted from this covariance matrix by eigenvalue decomposition.

By reordering the eigenvalues in descending order, a representation of the original data set can be constructed where the first principal component (highest eigenvalue) captures the largest variance in the data set and the lowest captures the least. In this way, PCA makes it possible to reduce the number of components needed to approximately recreate the original data set. That is, by applying PCA and discarding all but the first few principal components (which tend to contain most of the useful discriminatory information in the data), it is possible to represent a highly correlated, high dimensional data set, such as a hyperspectral data cube in a lower dimensional space. This, in turn, quickens processing analysis and classification [21].
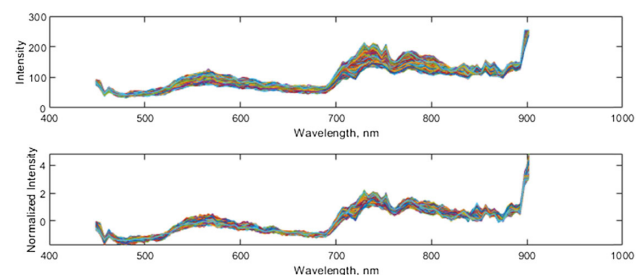

Fig. 11.   Effect of SNV on a set of spectra, normalized spectrum with reduced noise and interference.

C. Support Vector Machines Testing—Data Prediction and Classification

The dimensionally reduced data set was partitioned into a training and testing set with random sampling. A subset (typically lower than 10%) of all spectra was selected to form a training set for a classifier, while the remaining data was used for testing the accuracy of the trained SVM [22]. For HSI data sets, SVMs are a common classification technique [23]. SVMs attempt to classify data into distinct groups by virtually drawing a maximum margin hyperplane between groups or clusters of data points.

Often the data is not linear and has to be separated using a kernel trick [24]. This shifts data into a higher dimension, allowing a separating hyperplane to be introduced to differentiate between clusters in the higher dimensional space. SVM classification is a binary technique; however, adopting a one- versus-all method allows for multiple groupings/clusters to be classified. SVM models have to be trained. By exposing the model to examples of groupings/classes, the model attempts to find an ideal solution by iteration. Using a trained model, the SVM can predict and classify previously unseen data into the classes selected during training. The algorithm for data analysis and classification of crop types and crop diseases was developed using two separate SVMs, each trained for each specific task.

D. Classification of Salad Leaves

The ROIs were extracted to distinguish between three types of salad leaves, namely, spinach, rocket, and lettuce and split into a
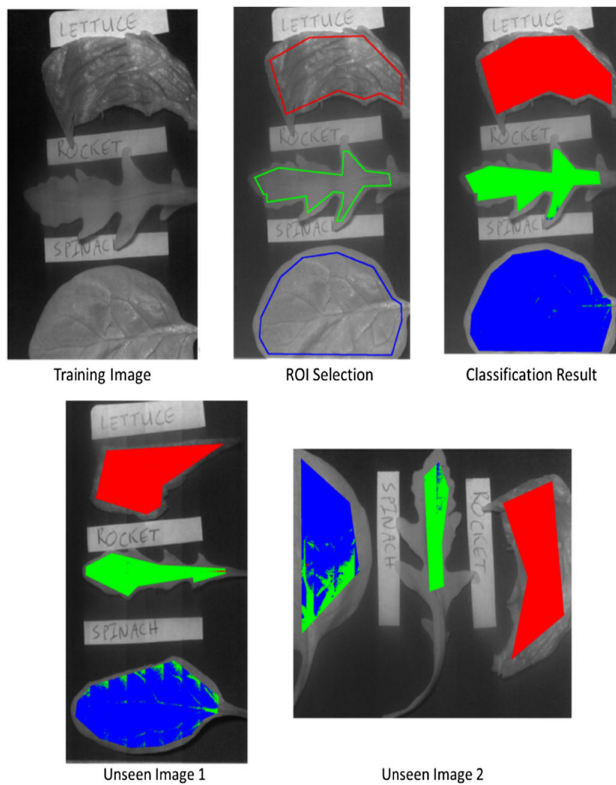

Fig. 12. Classification of salad leaves with accuracy using the decision/classification algorithm. Demonstrating the camera distinguishing differences in similar leaf types.

Table 3. Results of the SVM Classifier on Unseen Images

Class	Training Image	Unseen Image 1	Unseen Image 2
Lettuce	99.99%	99.97%	100.00%
Rocket	99.64%	99.43%	96.54%
Spinach	99.27%	92.59%	78.12%

test set and a training set. The training data was used to train an SVM before it was applied to the set of test data extracted from the HCC hyperspectral data cubes. The accuracy of the classification algorithm was evaluated on the test set. PCA was used for dimensionality reduction and feature extraction. The SVM used the radial basis function (RBF) kernel and selected the optimal parameters grid search using k-fold cross-validation. The results of the SVM classifier are shown in Fig. 12, and accuracies are reported in Table 3.

Aside for some visible confusion between spinach and rocket, the SVM classifies the individual types of salad leaves very effectively. This implies that the clusters of data are separable and that the SVM-based model is highly accurate.

E. Classification of Healthy and Unhealthy Potato Crops

To classify late blight in a potato crop, both healthy and diseased leaves were collected and mounted on a black card background for imaging. The data provided from his imaging was subject to the same analysis procedure, both pre- and post-processing. Using a subset of the data as training and testing data by random sampling, an SVM was trained and applied for classification of spectra from healthy and diseased leaves.

Once trained, the model was applied to classify the test data, which contained both healthy leaves and some displaying symptoms of blight. The results from one of the experiments are shown in Fig. 13, where the leaves in the top left image are healthy and the leaves in the top right image are diseased. For training, 10% of pixels in two leaves from each set were used to train the SVM to recognize the spectra of healthy/unhealthy leaves before using it to classify each of the leaves.

The leaves are mostly classified correctly; if a majority voting approach was used, each would be classified entirely as healthy or unhealthy based on the dominant class. In the previous examples, the majority of each leaf was showing healthy or unhealthy characteristics.

In the leaves taken from a different variety, small regions were displaying signs of blight. One such region was selected as the unhealthy training data, and a balanced number of pixels was selected to be the healthy training data. Again, these samples were used to train a model using an SVM, which was used to classify the rest of the testing pixels.

The results of this classification are shown in Fig. 14. This resulted in 88% accuracy in discriminating between healthy and unhealthy pixels. Given that several of the infected plants imaged were not symptomatic at the time of imaging, this level of accuracy is promising. It indicates that the HCC can be used to detect crop pathogen infection at an early stage, enabling time for treatment and avoidance of crop yield loss.
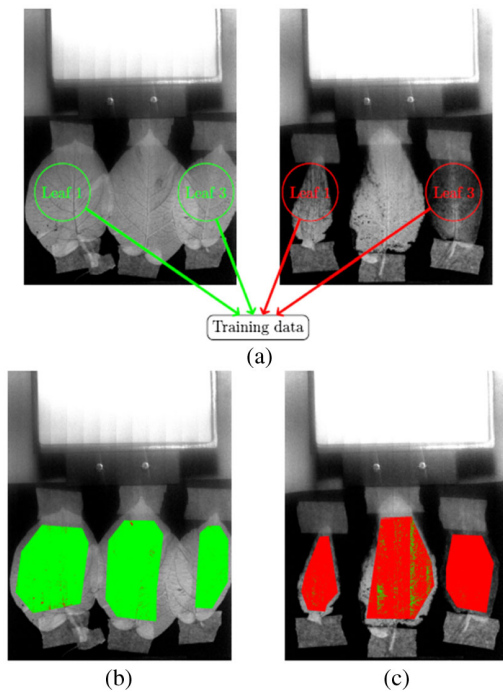
Fig. 13.   Supervised classification of the HCC image of potato leaves from a trial plot (plot 6) using a trained SVM.
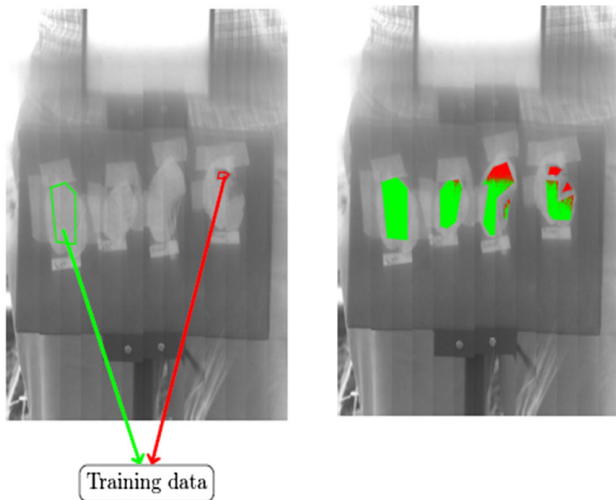

Fig. 14.   Supervised classification of the HCC image of potato leaves from a trial plot (plot 20) using a trained SVM.

5. CONCLUSION

A cost-effective visible-to-near-infrared LVF was developed using novel custom deposition mask design [10]. This enabled volume production of LVFs (around 800 LVFs per single process run; the major costs involved are targets used, substrates, process gasses, electricity usage, and labor) with controlled thickness distributions. These LVFs, in conjunction with a suitable detector system, can reduce costs, weight, and size. A low-cost HSI camera was manufactured using the developed LVFs, with performance comparable with commercial alternatives. This provides a high price-to-performance value proposition.

Compared to a high-end pushbroom HSI with similar specifications, the HSI prototype camera was comparable while only costing approximately 10% of the reference system.

The total volume of the portable, handheld prototype is 150 mm × 120 mm × 100 mm, and it weighs 650 g. An algorithm for the HCC system shows good feature extraction and SVM classification between similar leaf varieties while also achieving ∼88% accuracy in discriminating healthy and late-blight-expressing classes of potato plant leaves. These results are promising for future applications of the low-cost HSI camera, including potential for aerial and satellite monitoring.

REFERENCES

1. S. Liaghat, R. Ehsani, S. Mansor, H. Z. M. Shafri, S. Meon, S. Sankaran, and S. H. M. N. Azam, "Early detection of basal stem rot disease (Ganoderma) in oil palms based on hyperspectral reflectance data using pattern recognition algorithms," Int. J. Remote Sens. **35**, 3427–3439 (2014).
2. G. Giovanelli, N. Sinelli, R. Beghi, R. Guidetti, and E. Casiraghi, "NIR spectroscopy for the optimization of postharvest apple management," Postharvest Biol. Technol. **87**, 13–20 (2014).
3. M. A. Shahin, S. Symons, and D. Hatcher, "Quantification of mildew damage in soft red winter wheat based on spectral characteristic of bulk samples: a comparison of visible-near-infrared imaging and near-infrared spectroscopy," Food Bioprocess Technol. **7**, 224–234 (2014).
4. J. R. Davis, *Heat-Resistant Materials* (ASM International, 1997).
5. S. Sankaran, L. Khot, and R. Ehsani, "Mid- and far-infrared imaging," in *Imaging with Electromagnetic Spectrum: Applications in Food and Agriculture* (2014), pp. 129–146.
6. B. Liu, Y.-M. Yue, R. Li, W.-J. Shen, and K.-L. Wang, "Plant leaf chlorophyll content retrieval based on a field imaging spectroscopy system," Sensors **14**, 19910–19925 (2014).
7. R. Vašát, R. Kodešová, L. Borůvka, A. Klement, O. Jakšík, and A. Gholizadeh, "Consideration of peak parameters derived from continuum-removed spectra to predict extractable nutrients in soils with visible and near-infrared diffuse reflectance spectroscopy (VNIR-DRS)," Geoderma **232–234**, 208–218 (2014).
8. A. Emadi, H. Wu, G. De Graaf, P. Enoksson, J. H. Correia, and R. Wolffenbuttel, "Linear variable optical filter-based ultraviolet microspectrometer," Appl. Opt. **51**, 4308–4315 (2012).
9. A. T. Laëtitia, F. Lemarquis, and M. Lequime, "Masking mechanisms applied to thin-film coatings for the manufacturing of linear variable filters for two-dimensional array detectors," Appl. Opt. **47**, 5706–5714 (2008).
10. S. Song and D. Gibson, "Apparatus and methods for depositing variable interference filters," Patent application number GB1702478.7 (15 February 2017).
11. H. Tang, J. Gao, J. Zhang, X. Wang, and X. Fu, "Preparation and spectrum characterization of a high quality linear variable filter," Coatings **8**, 308 (2018).
12. A. Piegari, J. Bulir, and A. K. Sytchkova, "Variable narrow-band transmission filters for spectrometry from space. 2. Fabrication process," Appl. Opt. **47**, C151–C156 (2008).

13. C. Williams, G. Rughoobur, A. J. Flewitt, and T. D. Wilkinson, "Single-step fabrication of thin-film linear variable bandpass filters based on metal-insulator–metal geometry," Appl. Opt. **55**, 9237–9241 (2016).

14. S. Song, C. Li, H. O. Chu, and D. Gibson, "Reactive dynamics analysis of critical Nb_2O_5 sputtering rate for drum-based metal-like deposition," Appl. Opt. **56**, C206–C210 (2017).

15. C. Li, S. Song, D. Gibson, D. Child, H. on Chu, and E. Waddell, "Modeling and validation of uniform large-area optical coating deposition on a rotating drum using microwave plasma reactive sputtering," Appl. Opt. **56**, C65–C70 (2017).

16. Y. V. Martynenko, A. V. Rogov, and V. I. Shul'ga, "Angular distribution of atoms during the magnetron sputtering of polycrystaline targets," Tech. Phys. **57**, 439–444 (2012).

17. R. J. Barnes, M. S. Dhanoa, and S. J. Lister, "Standard normal variate transformation and de-trending of near-infrared diffuse reflectance spectra," Appl. Spectrosc. **43**, 772–777 (1989).

18. Å. Rinnan, F. Van Den Berg, and S. B. Engelsen, "Review of the most common pre-processing techniques for near-infrared spectra," TrAC Trends Anal. Chem. **28**, 1201–1222 (2009).

19. H. Abdi and L. J. Williams, "Principal component analysis," WIREs Comput. Stat. **2**, 433–459 (2010).

20. J. Ren, J. Zabalza, S. Marshall, and J. Zheng, "Effective feature extraction and data reduction in remote sensing using hyperspectral imaging [Applications Corner]," IEEE Signal Process. Mag. **31**(4), 149–154 (2014).

21. J. Zabalza, J. Ren, M. Yang, Y. Zhang, J. Wang, S. Marshall, and J. Han, "Novel folded-PCA for improved feature extraction and data reduction with hyperspectral imaging and SAR in remote sensing," ISPRS J. Photogr. Remote Sens. **93**, 112–122 (2014).

22. T. Rumpf, A. K. Mahlein, U. Steiner, E. C. Oerke, H. W. Dehne, and L. Plümer, "Early detection and classification of plant diseases with support vector machines based on hyperspectral reflectance," Comput. Electron. Agri. **74**, 91–99 (2010).

23. F. Melgani and L. Bruzzone, "Classification of hyperspectral remote sensing images with support vector machines," IEEE Trans. Geosci. Remote Sens. **42**, 1778–1790 (2004).

24. T. Hofmann, B. Schölkopf, and A. J. Smola, "Kernel methods in machine learning," Ann. Stat. **36**, 1171–1220 (2008).